Corrosion Science 236 (2024) 112248

Contents lists available at ScienceDirect

Corrosion Science

journal homepage: www.elsevier.com/locate/corsci

High-temperature hot corrosion kinetics of PVD $Ti_{1-x}Al_xN$ coatings on Nimonic c-263

O.E. Hudak [a,*], A. Scheiber [a], P. Kutrowatz [a], T. Wojcik [a], R. Hahn [a], J. Ramm [b], O. Hunold [b], S. Kolozsvári [c], P. Polcik [c], H. Riedl [a,d]

[a] Christian Doppler Laboratory for Surface Engineering of high-performance Components, TU Wien, Austria
[b] Oerlikon Balzers, Oerlikon Surface Solutions AG, Balzers FL-9496, Liechtenstein
[c] Plansee Composite Materials GmbH, Lechbruck am See D-86983, Germany
[d] Institute of Materials Science and Technology, TU Wien, Wien A-1060, Austria

ARTICLE INFO

Keywords:
Physical vapor deposition
Hot corrosion
Cathodic arc evaporation
High-temperature oxidation
TiAlN
Protective coatings

ABSTRACT

The high-temperature hot corrosion (HTHC) behavior of $Ti_{1-x}Al_xN$-coated c-263 alloy was studied with- and without a $Na_2SO_4/MgSO_4$ salt mixture at 850 °C in a SO_x-rich atmosphere. In absence of the salt deposit, both, the bare c-263 alloy and cathodic arc evaporated $Ti_{1-x}Al_xN$ specimens follow a quasi-cubic corrosion rate. However, when exposed to salt under identical conditions, the rates increase significantly, featuring a compounded parabolic-linear rate law for the c-263 alloy, and a parabolic-like rate behavior for $Ti_{1-x}Al_xN$-coated specimens. The rate-determining step of the HTHC mechanism was attributed to a nitride-to-oxide transformation, followed by a sequential fluxing of the formed oxides.

1. Introduction

In an attempt to improve the efficiency and robustness of gas turbines, engineers are constantly developing new strategies to increase the in-service jet temperature [1,2]. For these purposes, high-temperature nickel-based superalloys have become an indispensable choice in gas turbine construction, due to their excellent mechanical properties at high temperatures [3–6]. Unfortunately, many of these high-temperature alloys are prone to accelerated salt-induced corrosion called hot corrosion (HC) [7–12]. Within a temperature range of 650–950 °C, formations of salt deposits elicit accelerated corrosion, which ultimately leads to a premature failure of high-cost components, such as transition lines of the combustion chamber, as well as blades and vanes of the high- and low-pressure turbine. It is for such applications that protective physical vapor deposited (PVD) coatings provide an attractive solution for extending the lifetime of highly stressed turbine elements. Many coating systems have demonstrated beneficial corrosion resistance in high temperature environments, such as MCrAlY [13–15], metallic gradient coatings [16], ceramic coatings [17–24], and enamel [25,26], but remain far from being optimal.

With a focus on industrially established Ni- and Co-based superalloys that readily find application in high-temperature settings, the objective of this study is to investigate the hot corrosion behavior of a Nimonic c-263 alloy at 850 °C and to improve its corrosion behavior through the application of protective cathodic arc evaporated [cae] $Ti_{1-x}Al_xN$ coatings. Furthermore, we aim to deepen the fundamental understanding of the respective HC rates and mechanisms.

Throughout the following sections, the authors would like to provide a condensed background around hot corrosion, high-temperature hot corrosion (HTHC), and the underlying chemical reaction mechanisms that are relevant to this study.

1.1. Hot corrosion

When sulfur from the kerosene (<0.3 m.%) is combusted, it oxidizes entirely and forms a mixture of SO_2 and SO_3 (SO_x), as shown by Eqs. 1–2 [27].

$$S + O_2 \rightarrow SO_2 \tag{1}$$

$$SO_2 + 1/2O_2 \quad + \frac{(M)}{catalyst} \leftrightarrow SO_3 \tag{2}$$

When operating in marine environments, salt-rich aerosols can enter the turbine sections through the air intake (e.g., Na^+, K^+, Mg^{2+}, Ca^{2+}),

* Corresponding author.
E-mail address: oliver.hudak@tuwien.ac.at (O.E. Hudak).

https://doi.org/10.1016/j.corsci.2024.112248
Received 16 May 2024; Received in revised form 21 June 2024; Accepted 30 June 2024
Available online 1 July 2024

where they react with the SO_x-rich exhaust gases and form high-melting sulfate salt deposits (Eqs. 3–4) [28,29].

$$2NaCl + S + 2O_2 \rightarrow Na_2SO_4 + Cl_2 \quad \text{Tm} = \quad 884 \quad ^\circ\text{C} \tag{3}$$

$$MgCl_2 + S + 2O_2 \rightarrow MgSO_4 + Cl_2 \quad \text{Tm} = \quad 1124 \quad ^\circ\text{C} \tag{4}$$

Hot corrosion is further subdivided into one of two corrosion mechanism, depending on the physical aggregate of the salt deposit,: High-temperature hot corrosion (HTHC, Type 1), where the salt deposit exits in a molten state, or low-temperature hot corrosion (LTHC, Type 2), where the deposit adheres as a solid.

This significantly complicates the study of hot corrosion phenomena in industrial settings, as both temperature and mole fractions of multi-component salt deposits substantially influence the predominant corrosion mechanism. For instance, while Na_2SO_4- and $MgSO_4$ deposits have melting points of 884 °C and 1124 °C, respectively, their binary system features a eutectic temperature of merely 665 °C [29]. Thus, components that operate at 850 °C and are exposed to either Na_2SO_4 or $MgSO_4$ individually would likely experience a LTHC attack, while surfaces exposed to the eutectic mixture of $Na_2SO_4/MgSO_4$ experience HTHC. In order to set the stage for investigating HTHC phenomena, strict measures were set throughout this study to ensure the proper corrosion environment. That is, isothermal annealing experiments were conducted at 850 °C in an SO_x-rich atmosphere with an 80 mol% $Na_2SO_4/MgSO_4$ salt mixture (T_m=~800 °C) to ensure the liquefaction of the salt deposit.

1.2. High-temperature hot corrosion

HTHC of metals and alloys may involve various degenerative processes: A sulfidation-oxidation mechanism [7,30–33] acidic or basic dissolution of the protective oxide scale (fluxing) [33–37] or a synergistic co-dissolution mechanism, referred to as synergistic fluxing. Whether or not conditions for sulfidation or fluxing are met depends on a material's chemical makeup, temperature profile, chemical composition of the atmosphere, and, as a result, on the melt basicity of the salt deposit.

In many instances, sulfur behaves much more aggressively than oxygen. Many metals such as iron (Fe), Nickel (Ni), Cobalt (Co), and Chromium (Cr) react readily with sulfur, achieving reaction rates that are several magnitudes higher compared to oxygen under the same conditions [35]. Reasons for the higher reaction rates for metal-sulfides include: (i) metal-sulfide formations that are accompanied by larger concentrations of lattice defects than their related metal-oxide variants. Consequently, diffusion rates in sulfides are significantly higher, allowing further sulfidation and oxygidation to ensue; (ii) many metal-sulfides feature low melting points. This is especially true for alloying elements used in Ni-based superalloys, such as Co and Fe, whose sulfides (Ni_3S_2, Co_4S_3, and FeS) have melting temperatures of 635 °C, 880 °C and 985 °C, respectively. Ni-sulfides also tend to form low-melting eutectics, which can further lower the liquidus line of the salt-deposit. Lastly, (iii) metal-sulfides exhibit much greater dissociation pressures than their metal-oxide counterparts. As a result, high sulfur partial pressures develop at the scale-metal interface, leading to accelerated intergranular corrosion [38].

Fluxing, on the other hand, describes the reaction between protective oxide scales and components of the salt deposit, by which the product barrier becomes non-protective and produces species that are soluble within the salt. When considering a melt of pure Na_2SO_4, it partially dissociates into its basic (Na_2O) and acidic (SO_3) components (Eq. 5). Depending on which species reacts with the protective oxide scale of a material, it is referred to as a basic or acidic fluxing mechanism.

$$Na_2SO_4 \leftrightarrow \quad Na_2O + \quad SO_3(diss.) \tag{5}$$

1.3. Salt-induced basic fluxing

Basic fluxing predominates typically at higher temperatures (~900 °C), where the production of O^{2-}-ions through decomposition of the salt melt is sufficiently high, and the acidic component of the atmosphere (e.g., SO_3) is negligible. Unlike acidic fluxing, basic fluxing is considered non-self-sustaining and ultimately depends on the amount of salt deposit available for the reactions. If, however, sufficient salt deposit is present, and therefore a sufficiently high reservoir of O^{2-}, a long-term investigation of such a basic fluxing mechanism is possible. In the event of basic dissolution of protective oxide scales, Na_2O (O^{2-}) in the liquid salt film reacts with the metal-oxide and forms soluble anionic species, leading to an accelerated deterioration of the scale.

2. Experimental

2.1. Coating depositions

Single-crystalline Si stripes (100-oriented, 20x7x0.38 mm) and Nimonic c-263 (VDM-Metals, Germany, Table 1) served as substrate materials for all $Ti_{1-x}Al_xN$ depositions. Whereas coated Si-substrates were solely utilized for coating-characterization purposes, such as analysis of the coating morphologies, coating thickness measurements, and crystal-phase determination by X-ray diffraction), the coated c-263 alloys were exclusively used for hot corrosion experiments and post-corrosion analysis.

Before deposition, the substrates underwent ultrasonic cleaning with acetone and ethanol before being mounted onto the carousel of the deposition chamber. At a base pressure of $< 5.0^{-3}$ Pa, the substrates underwent further cleaning for 25 min by means of a central-beam argon plasma etching procedure (Oerlikon Surface Solutions AG).

All coatings were deposited using an industrial-scale cathodic arc evaporation system (Oerlikon Innova 1.0, Oerlikon Surface Solutions AG). The $Ti_{1-x}Al_xN$ coatings were reactively grown on the top-face of the substrates in a pure N_2 atmosphere at a total pressure of 3.2 Pa. With a DC bias of −40 V and 480 °C substrate temperature, a total of six sources were operated with target current of 200 A. Equipped with either TiAl (50/50 at%) and TiAl(35/65 at%) targets (Plansee Composite Materials GmbH) two ~10 μm thick coating variants with varying Al contents ($Ti_{0.52}Al_{0.48}N$ and $Ti_{0.34}Al_{0.66}N$, respectively) were deposited with a deposition rate of 9.8 nm·min^{-1} per source.

2.2. Hot corrosion experiments

All hot corrosion experiments were conducted using an in-house built corrosion rig, comprised of a gas-mixing module (inlet), a quartz-tube (reaction chamber), a three-zone gradient furnace, and a gas-treatment system (outlet). A detailed description and illustration of the HC-testing rig can be found in [40].

For each corrosion experiment, two sets of sample arrangements were evaluated: (i) a control configuration, where no salt was introduced onto the sample surfaces, and (ii) an experimental arrangement, where samples were prepared with salt coupons to replicate hot corrosion conditions.

A blend of anhydrous $MgSO_4$ and Na_2SO_4 (Merck KGaA) in a molar ratio of 20:80, respectively, was selected for all experiments. The mixture was then dissolved in water to create a saturated solution. Subsequently small droplets were dispensed onto the sample surfaces using a pipette and left to dry under ambient conditions for several days, producing salt-deposits exhibiting an average mass of 142±27 mg covering an area of aproximately 0.6 cm^2. By reference to the calculated binary-phase diagram from Yazhenskikh et al., an approximate solidus temperature of 725 °C and a liquidus temperature of around 810 °C were projected for the fabricated salt coupons. These estimations were subsequently validated through a sequence of annealing experiments [29].

Once the quartz tube was loaded with both the control arrangement

Table 1
Nominal chemical composition (wt%) of the Nimonic c-263 superalloy.

	Ni	Co	Cr	Mo	Ti	Al	Fe	Si
Nimonic c-263 [39]	47–54	19–21	19–21	5.6–6.1	1.9–2.4	0.3–0.6	0–0.7	0–0.4

and the salt-loaded samples, the chamber was sealed and purged for 10 min with Ar. Subsequently, the furnace was switched on while Ar purging continued. 45 min were the allocated to reaching the desired temperature of 850 °C at a ramp-rate of 20 °C/min, followed by an additional 15 minutes to ensure uniform temperature distribution within the quartz tube. Upon completion of the heat-up sequence, a SO_2-rich atmosphere ($p_{[Ar]}= 8.47\times10^{-1}$ atm, $p_{[O2]}= 1.5\times10^{-1}$ atm and $p_{[SO2]}=2.8\times10^{-3}$ atm) was introduced, marking the onset ($t_{0\,h}$) of the corrosion experiment. Once the desired duration of the experiment had elapsed (e.g., t=1, 5, 15, and 30 h), the furnace was switched off, and the chamber was purged anew with Ar until the temperature within the quartz tube dropped below 200 °C, marking the end of the corrosion experiment.

2.3. Analytical methods

For characterizing the as-deosited morphology of the coatings, as well as coaing thickness, and quality of substrate-coating interfaces, a Zeiss Sigma 500 VP high-resolution field emission gun scanning electron microscope (FEGSEM) was employed. Equiped with an EDAX Octane elect system, energy dispersive X-ray spectroscopy (EDX) was utilized for quantative elemental investigations. To increase accuracy of the measurments, the EDX system was calibrated with coating standards and cross-referenced using Elastic Recoil Detection Analysis (ERDA).

For crystallographic analysis, Bragg-Brentano X-ray diffraction (BBHD) was utilized by means of a PANalytical XPert Pro MPD system equipped with a Cu-Kα radiation source (wave length λ =1.54 Å).

For post-corrosion investigations, top-view images were captured using a digital light microscope. Sample surfaces were the carefully rinsed with distilled water to rid them from any residual salt-deposits (if needed) and subsequently prepared for BBHD XRD analysis. Thereafter, the samples were embedded in a conductive polymer matrix and their cross-sections ground, polished, and examined using a Zeiss Sigma 500 VP high-resolution FEGSEM. EDX line-scans were conducted to compile diffusion profiles, and examine the corrosion and scaling behavior of the coatings.

Lastly, transmission electron microscopy (TEM) was performed using a FEI TECNAI F20 equipped with a field emission and an accelerating voltage of 200 kV. Bright-field (BF) imaging, as well as selected area electron diffraction (SAED) were consulted to gain detailed insights into the microstructure, diffusion processes, and corrosion mechanism. To prepare the TEM lamella, a standardized focused-ion beam (FIB) lift-out technique was employed using a Scios 2 DualBeam system from ThermoFisher Scientific.

3. Results

3.1. Structure and morphology

Fracture cross-sections of the as-deposited low Al-content $Ti_{0.52}Al_{0.48}N$ and high Al-content $Ti_{0.34}Al_{0.66}N$ coatings are shown in Fig. 1a and b, respectively. Both coating variants exhibit a uniform and dense columnar microstructure with thicknesses of 9.8 µm ($Ti_{0.52}Al_{0.48}N$) and 10.1 µm ($Ti_{0.34}Al_{0.66}N$). The EDX analysis revealed that the chemical compositions of the $Ti_{0.52}Al_{0.48}N$ and $Ti_{0.34}Al_{0.66}N$ coatings, adjusted to the metallic sublattice, show only minor deviations from their intended compositions (50/50 and 35/65 at%, respectively). XRD structural analysis indicates a prevailing c-Ti(Al)N crystal structure (B1, NaCl-prototype) for both coatings, with only faint indications of the thermodynamically favored h-Al(Ti)N phase (B4, wurzite-prototype)

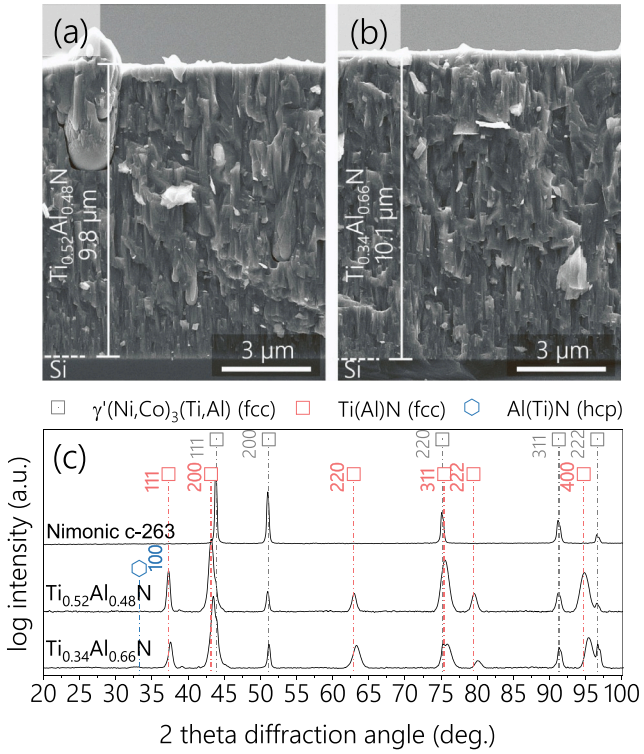

Fig. 1. As-deposited characterization of cae-$Ti_{1-x}Al_xN$: (a-b) show fracture cross-sections of the $Ti_{0.52}Al_{0.48}N$ and $Ti_{0.34}Al_{0.66}N$ deposited on Si, respectively, whereas (c) exhibits XRD diffractograms of their crystal structure. Reprinted under the CC-BY license from Elsevier (Fig. 1 from O. E. Hudak et. al., Ref. [40]).

observed for the $Ti_{0.34}Al_{0.66}N$ coating with higher Al content (Fig. 1c).

Fig. 2 displays top-view images of all samples subjected to hot corrosion experiments. All samples underwent exposure to an identical corrosive atmosphere and were annealed at 850 °C with a partial pressure of $p_{[SO2]}= 2.8\times10^{-3}$ atm (2800 ppm by volume). Presented Fig. 2a is the control group (salt-free samples), consisting of the uncoated c-263 alloy, $Ti_{0.52}Al_{0.48}N$, and $Ti_{0.34}Al_{0.66}N$ coated samples, listed from top to bottom. A progressive alteration in interference colors is noticeable, corresponding to the development of oxide scales.

In Fig. 2b, the surfaces of the salt-loaded samples are shown in their as-deposited state (0 h) and after corrosion times of 1, 5, 15, and 30 h. The molten salt deposit prerequisite is clearly met and provides the foundation for high-temperature hot corrosion (HTHC). Significant uptake (consumption) of the salt deposit can be seen for the uncoated NiCrCo alloy, which is indicative of significant corrosion. During the first hour, the salt deposit melts and adheres to the alloy surface. A brown oxide scale develops at the bare alloy surface, identified as a mixed NiO-Cr_2O_3 oxide scale. As the corrosion experiment progresses, a gradual depletion of the salt deposit is observed (5–15 h). After 30 h, the entire salt deposited has been consumed by the alloy, which is now covered with a porous corrosion scale.

In constrast, the corrosion progression and depletion of the salt deposit for the $Ti_{1-x}Al_xN$ coated specimens occur much slower. First, clear indications of salt uptake can be seen after 15 h for the $Ti_{0.52}Al_{0.48}N$ coated samples. Significant scaling and spalling of the surface oxides can

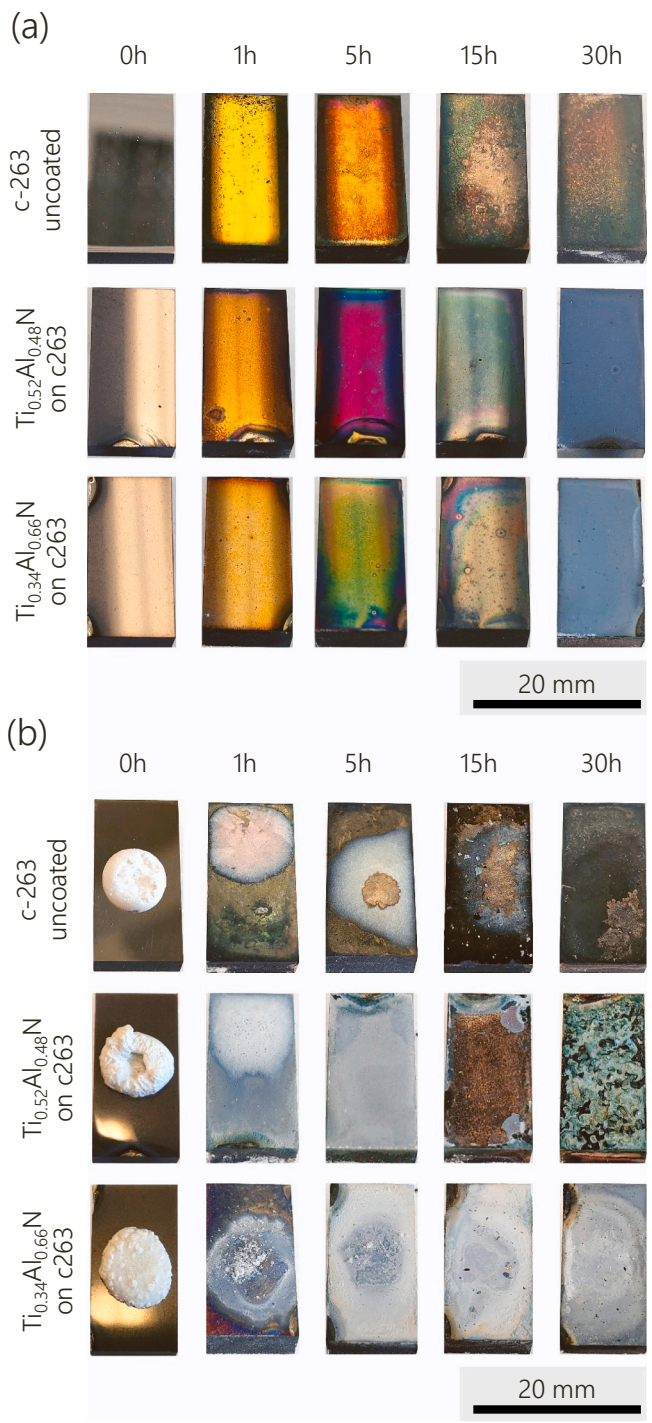

Fig. 2. Top-view images depict samples annealed at 850 °C in a SO_x-rich atmosphere: (a) without salt deposits for 0, 1, 5, 15, and 30 h, as well as (b) with salt deposits under identical conditions. Pertaining to both (a) and (b), the first row features uncoated Nimonic c-263 substrates, while the second and third rows show $Ti_{0.52}Al_{0.48}N$ and $Ti_{0.34}Al_{0.66}N$ coated c-263 substrates, respectively.

be seen after a corrosion duration of 30 h. Especially, the $Ti_{0.34}Al_{0.66}N$ coated samples feature minor salt uptake throughout 30 h of the corrosion experiments. It could be argued that the notable depletion of the deposit seen in the $Ti_{0.52}Al_{0.48}N$ sample is indicative for a breach in the coating structure, allowing the salt to penetrate the protective layer and react with the c-263 substrate below.

3.2. Structural evolution of annealed $Ti_{1-x}Al_xN$ in SO_x-enriched atmosphere

To gain insights into the formation of corrosion products throughout the HTHC experiments, structural analysis by XRD was conducted. Fig. 3a presents the structural evolution of the salt-free $Ti_{0.52}Al_{0.48}N$ and $Ti_{0.34}Al_{0.66}N$ coatings annealed at 850 °C in a 2800 ppm SO_x-rich atmosphere. In contrast, Fig. 3b features the structural evolution for the salt-loaded samples, annealed under identical atmospheric conditions. For reference purposes, the diffractograms of the as-deposited coating states are included.

Starting with the salt-free $Ti_{0.52}Al_{0.48}N$ coating, immediate onset of fast-growing tetragonal-TiO_2 anatase and rutile oxides is observed after 1 h exposure time, which is accompanied by a phase transition from the c-Ti(Al)N to the thermodynamically favored h-Al(Ti)N (Fig. 3a). Also apparent is the development of an Al-O-phase, which will crystalize into r-Al_2O_3 as the annealing duration is prolonged. More distinct reflexes are measured between 1 h and 30 h, suggesting further development of each aforementioned oxide. Notably, the contribution of rutile-TiO_2 and r-Al_2O_3 phases seem to gain dominance throughout the oxide scale, indicated by the relative intensities and the receding anatase-TiO_2. Similar to the salt-free $Ti_{0.52}Al_{0.48}N$, the higher Al-content salt-free $Ti_{0.34}Al_{0.66}N$ instantaneously forms a mixed-oxide scale within 1 h at 850 °C, evident from the rutile-TiO_2, anatase-TiO_2 and r-Al_2O_3 diffraction peaks.

For both compositions, further annealing at 850 °C leads to thermally induced spinodal decomposition of the c-$Ti_{1-x}Al_xN$ solid solution, which is accompanied by the precipitation of coherent AlN particles. By reference to the preferential [200]-reflex at 43.27°, an unmixing of the c-TiAlN solid solution into Ti-rich c-Ti(Al)N and metastable Al-rich c-Al(Ti)N domains occurs, which we interpret according to the peak-broadening of the initial (as-deposited) c-Ti(Al)N [200]-reflex. As the $Ti_{0.34}Al_{0.66}N$ chemistry falls closer to the solubility limit of c-Ti(Al)N, more pronounced w-AlN formation is prevalent throughout the annealing experiments. Despite literature reporting significantly higher temperatures (>1000 °C) as a precondition for w-AlN nucleation, the [100]-reflex positioned at 33.18° in Fig. 3a provides a significant argument that nucleation and growth of w-AlN in supersaturated c-Ti(Al)N coatings may already form at much lower temperatures (850 °C). This, in fact, has also been observed by Rogström et al. in a series of in-situ high-energy X-ray diffraction (XRD) experiments while studying microstructure and the strain evolution during decomposition [41]. This discrepancy may be due to the significantly longer annealing time.

The structural evolution of the $Ti_{0.52}Al_{0.48}N$ and $Ti_{0.34}Al_{0.66}N$ coatings after 30 h of annealing at 850 °C in an SO_2-enriched atmosphere without salt deposits can be summarized as follows: Both coatings develop a fast-growing mixed TiO_2/Al_2O_3 oxide scale, where the TiO_2 phases consist of both, rutile and anatase. Judging from the relative peak intensities, the scale formation for the lower Al-containing $Ti_{0.52}Al_{0.48}N$ coating seems to be TiO_2 dominated, whereas a more balanced contribution between TiO_2 and Al_2O_3 exists for the higher Al-containing $Ti_{0.34}Al_{0.66}N$ coating. Lastly, significant nucleation and growth of w-Al(Ti)N and spinodal decomposition of the c-Ti(Al)N solid solution are observed throughout the annealing experiments for the high Al-content $Ti_{0.34}Al_{0.66}N$ coating.

On the other hand, the structural evolution for salt-loaded $Ti_{1-x}Al_xN$ coatings is much more dynamic (see Fig. 3b). After 1 h, a significantly pronounced scale formation can be seen. Distinct diffraction intensities of the r-TiO_2 and a-TiO_2 structure, as well as an onset of the r-Al_2O_3 structure, are featured by both coating variants. Again, the Al_2O_3 contribution is more dominant for the higher Al-containing $Ti_{0.34}Al_{0.66}N$ coating. Moreover, the thermally unstable tialite structure (o-$TiAl_2O_5$) develops throughout the first 5 h of the salt-loaded experiments as one of the dominant structural constituents of the developing oxide scale. As the annealing duration is prolonged, the initially fast-growing tialite phase decompose into its parent oxides, alumina and rutile.

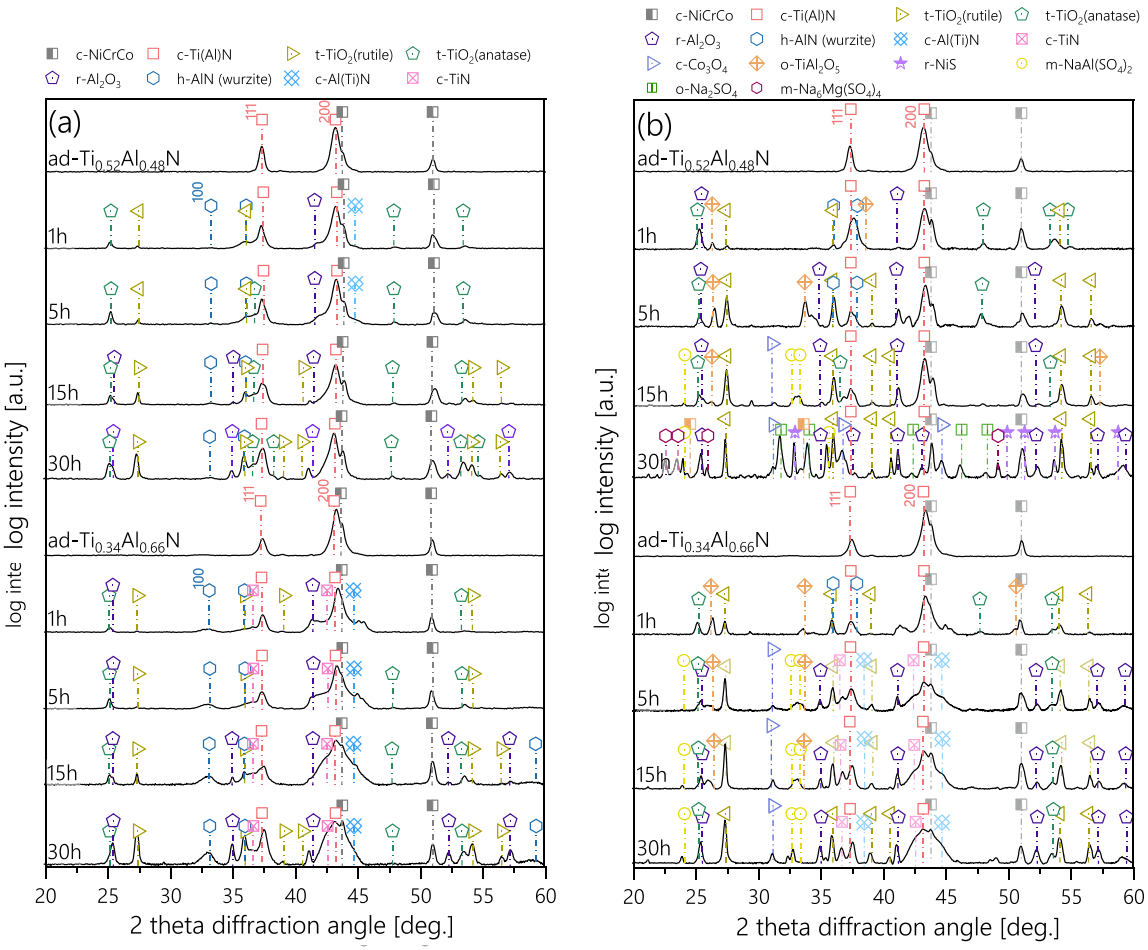

Fig. 3. Crystal structure analysis of $Ti_{0.52}Al_{0.48}N$ and $Ti_{0.34}Al_{0.66}N$ coatings annealed in an SO_x-rich atmosphere at 850 °C (a) without salt deposits and (b) with salt deposits [41–53].

3.3. Oxidation and corrosion kinetics in SO_2-rich atmosphere

Since HTHC most often occurs in the presence of a SO_x-enriched atmosphere, all annealing and corrosion experiments were performed at a partial pressure of $p[SO_2] = 2.8\times10^{-3}$ atm (2800 ppm by volume). In order to describe the oxidation behavior for such an environment, annealing experiments were first conducted without any salt deposits to determine the oxygen diffusion kinetics experimentally. Over periods of 1, 5, 15, and 30 h, $Ti_{1-x}Al_xN$ coated, as well as uncoated NiCoCr samples were annealed at temperatures of 700, 775, and 850 °C– temperatures, where HTHC begins to play a factor. Depth profiles for the oxygen inward diffusion were obtained by conducting EDX line scans along the cross-section of each annealed sample and are shown in Fig. 4(a-i).

Material-specific diffusion rate laws were determined by plotting the diffusion depth over time. A quasi-cubic rate function (n=~3) was found to best fit the oxygen inward diffusion for the NiCrCo c-263 alloy, the $Ti_{0.52}Al_{0.48}N$ and $Ti_{0.34}Al_{0.66}N$ coated samples at each annealing temperature (Figs. 4j, 4k and 4 l, respectively). In Eq. 8, the generic rate law is described, where x refers to the distance, d_{ox} to the rate constant, t corresponds to the time, and n is a constant.

$$x_{ox}^{n} = d_{ox} \bullet t \tag{8}$$

The rate law allows for determining temperature-dependent rate constants (d_{ox}), which can be plotted in an Arrhenius plot (Eq. 9) to further describe the oxygen diffusion kinetics. By plotting the ln function of the Arrhenius plot, the pre-exponential factors ($d_{0\ ox}$) could be determined from the intersection of the linear fit with the ordinate, and the activation energies (q_{ox}) were derived from the slope.

$$d_{ox} = d_{0ox} \bullet e^{\frac{q_{ox}}{RT}} \tag{9}$$

$$\ln(d_{ox}) = -\frac{q_{ox}}{R} \bullet \frac{1}{T} + \ln(d_{0ox}) \tag{10}$$

where d_{ox} denotes the mean diffusion rate, $d_{0\ ox}$ the pre-exponential factor, q_{ox} the activation energy, R the gas constant, and T the temperature.

The derived activation energies for oxygen follow the order of $Q_{(c\text{-}263)} < Q_{(Ti0.36Al0.66\ N)} < Q_{(Ti0.52Al0.48\ N)}$ (Table 2) and fall significantly lower to literature values that have been calculated from annealing experiments conducted in air. Particularly, the uncoated c-263 alloy shows a drastic reduction in the Q_a-value when SO_2 is present in the atmosphere (Q_a=51 kJ/mol) compared to pure air exposure (~110 kJ/mol) [54]. This may be due to two key reasons: (i) a not sufficiently evolved native oxide scale prior to the annealing experiments, where the alloy was in a polished state. Higher diffusion rates are thus observed during the first hour of the annealing experiments, where a passive scale is still developing. (ii) SO_2 acts as a reducing agent. It is well understood that SO_2 may further oxidize to SO_3 in an oxidizing atmosphere such as air (homogeneous conversion), which is thermodynamically favored at lower temperatures [55,56]. Moreover, fly ash or metal oxide surfaces on turbine components can lead to catalytic effects that accelerate the conversion of SO_2 to SO_3 (heterogeneous conversion) [56–58]. We associate this latter case with the drop in activation energies derived throughout the annealing experiments of this study. Thus, elevated SO_2 concentrations can considerably restrict the ability to thermally grow a

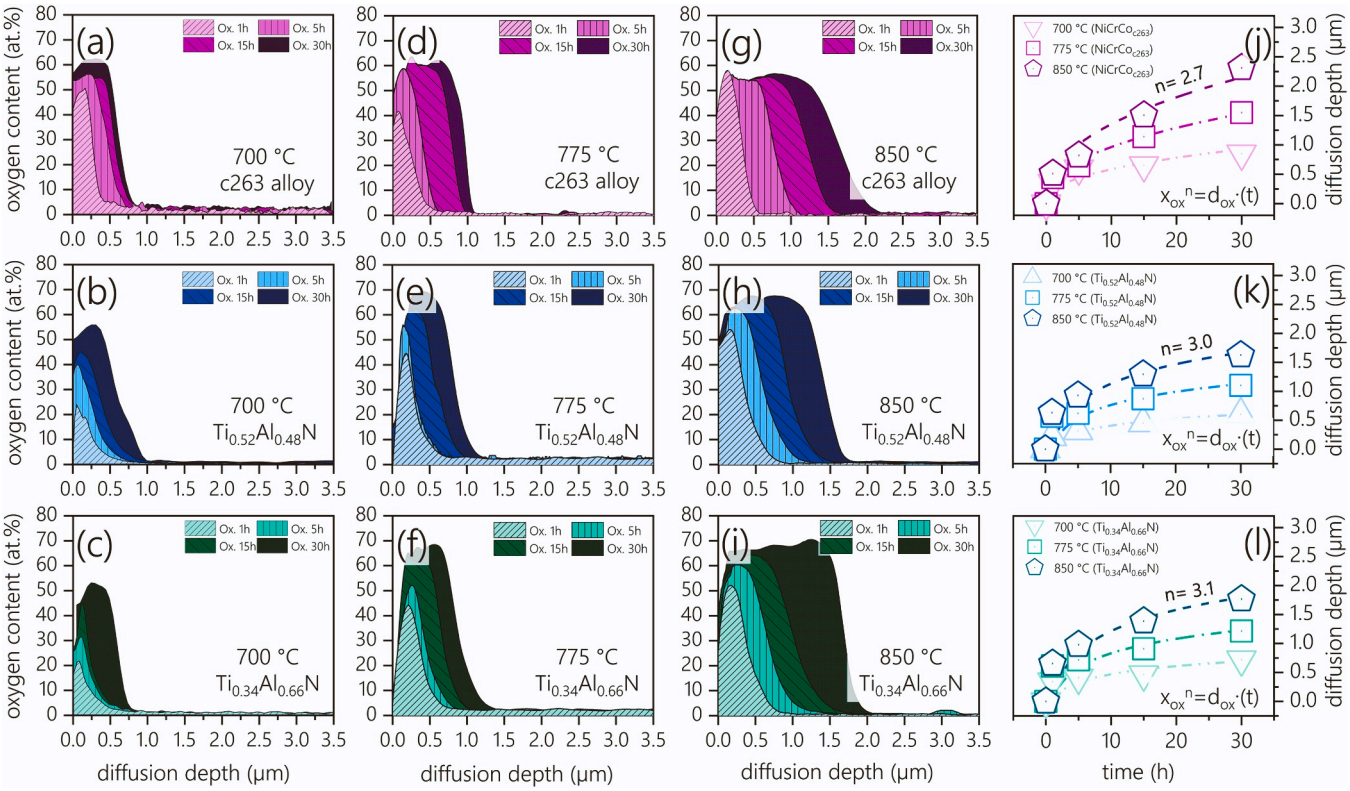

Fig. 4. (a-i) show oxygen diffusion profiles of bare c-263 alloy, $Ti_{0.52}Al_{0.48}N$ and $Ti_{0.36}Al_{0.66}N$ coated samples that have been annealed at 700, 775, and 850 °C in a SO_x-rich atmosphere for 1, 5, 15 and 30 h without salt deposits. (j-k) feature graphical representations of the oxygen diffusion profiles, manifesting the diffusion rate laws and related rate constants (d_{ox}), which best pertain to each sample.

Table 2
Shows the logarithmic rate constants (d_{ox}) for the oxygen inward diffusion of $Ti_{0.52}Al_{0.48}N$, $Ti_{0.34}Al_{0.66}N$ and the parabolic-like rate constants ($d_{ox,n=2.38}$) for the uncoated c263 at 700, 775, and 850°C. Moreover, pre-exponential factors ($d_{0\ ox}$) and activation energies (Q_{ox}) are provided, which have been derived with respect to the diffusion coefficients.

T (°C)	$Ti_{0.52}Al_{0.48}N$			$Ti_{0.34}Al_{0.66}N$			c-263 alloy		
	d_{ox} cm^n/h	$d_{0\ ox}$ cm^n/h	Q_{ox} kJ/mol	d_{ox} cm^n/h	$d_{0\ ox}$ cm^n/h	Q_{ox} J/mol	d_{ox} cm^n/h	$d_{0\ ox}$ cm^n/h	Q_{ox} (kJ/mol)
700	$1.89{\cdot}10^{-5} \pm 3.90{\cdot}10^{-7}$	$4.32{\cdot}10^{-2}$	62.3	$2.25{\cdot}10^{-5} \pm 1.57{\cdot}10^{-6}$	$2.97{\cdot}10^{-2}$	57.9	$2.57{\cdot}10^{-5} \pm 2.07{\cdot}10^{-6}$	$1.41{\cdot}10^{-2}$	51.1
775	$3.56{\cdot}10^{-5} \pm 1.98{\cdot}10^{-7}$			$4.00{\cdot}10^{-5} \pm 1.17{\cdot}10^{-6}$			$4.21{\cdot}10^{-5} \pm 2.04{\cdot}10^{-6}$		
850	$5.27{\cdot}10^{-5} \pm 4.98{\cdot}10^{-7}$			$5.84{\cdot}10^{-5} \pm 3.68{\cdot}10^{-7}$			$5.94{\cdot}10^{-5} \pm 5.25{\cdot}10^{-6}$		

passive oxide scale to function as an oxygen diffusion barrier, whether this entails the formation of a Cr_2O_3/NiO dominated scale (c-263 alloy) or a mixed TiO_2/Al_2O_3 scale ($Ti_{1-x}Al_xN$ coatings).

Lastly, the oxidation rate law constants (n) were determined for the salt-loaded HTHC sample group at 850 °C. Unlike the derivations of the activation energies calculated across a temperature range (700–850 °C), the oxygen rate constants for the salt-loaded corrosion experiments were solely conducted at 850 °C. The reason for this is the prerequisite for a molten salt film, which would not be met at lower temperatures. Presented in Fig. 5 are the diffusion depth-time plots for the salt-loaded and salt-free samples that were annealed at 850 °C. While the samples without salt deposit exhibit fairly similar oxidation kinetics– as previously described by their activation energies and quasi-cubic diffusion rate laws– the oxidation rates drastically change when salt is introduced.

Firstly, the oxidation rate law of the c-263 alloy changes from a quasi-cubic rate law (n=2.7) when exposed to a SO_x-rich atmosphere towards a compounded parabolic-linear rate law (n=1.5) when salt deposits are added. For the latter case, a parabolic oxidation behavior governs the first few hours of the corrosion experiments (0–15 h), after which a linear oxidation rate takes over. Such linear rates are characteristic of HTHC of high-temperature alloys and essentially motivate the application of protective coatings [59–61].

In contrast to the uncoated c-263 alloy, the oxidation rate laws for both, $Ti_{0.52}Al_{0.48}N$ and $Ti_{0.34}Al_{0.66}N$ coated samples change from a cubic-diffusion rate (n= 3.0 and 3.1, respectively) to a near-parabolic rate behavior with n=2.3 and n= 2.2, respectively (see Fig. 5).

3.4. HTHC mechanism for $Ti_{1-x}Al_xN$ coatings

Over the last few decades, a general understanding has evolved around the behavior and stability of various metals and their oxides when exposed to sulfate salts at high temperatures. Particularly, Na_2SO_4 has stood at the forefront of many hot corrosion studies, due to its relatively high thermal stability, ability to form low melting mixtures

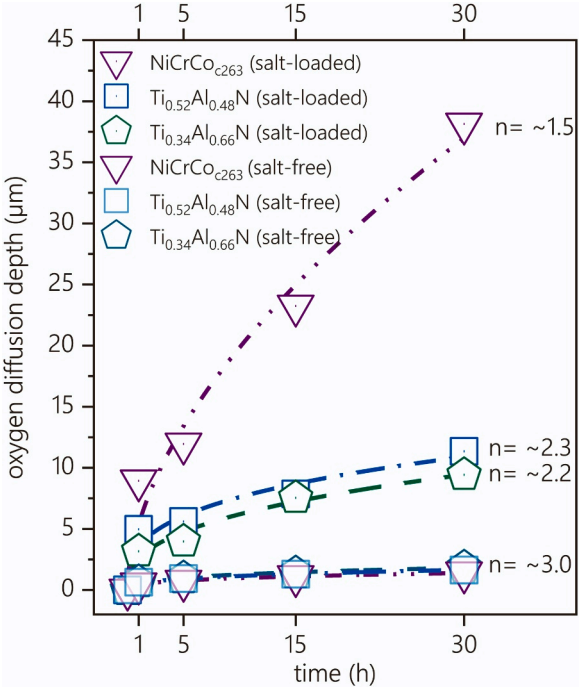

Fig. 5. Oxidation kinetics of uncoated c-263 alloy and $Ti_{1-x}Al_xN$ coated samples, featuring the diffusion depth-time plot used for determining the corrosion rates of salt-loaded and salt-free samples at 850 °C in an SO_x-rich atmosphere.

with other salts, and its presence and relevance in many high-temperature applications. However, little knowledge exists about the stability and behavior of metal nitrides in conjunction with Na_2SO_4 deposits at high temperatures. For this reason, this section intends to provide a time-resolved description of the stability of cae-$Ti_{1-x}Al_xN$ coatings when brought in contact with a Na_2SO_4-based salt mixture (80 mol% Na_2SO_4-$MgSO_4$) at 850 °C.

In general, the high-temperature hot corrosion mechanism can be subdevided into four key stages, which delineate the chronological sequence in which alloys and coatings will degrade over time [62]:

I. Incubation: In absence of a salt deposit, the incubation stage comprises the formation of a stable passive oxide scale, which ptrotects the alloy or coating from further oxidation.
II. Initiation: Next, the initiation stage encompsases a series of changes in the material's environment, which facilitate aggressive conditions where further oxidation and/or degradation of the oxide scale occurs. This includes the deposition of a salt deposit, its melting (transition from solid deposit to liquid film), fluctuations in the melt-basicity, and depassivation of the protective scale.
III. Propagation: Describes an accelerated depassivation of the protective metal oxide scale followed by an accelerated attack of the underlying resitdual coating or alloy and precipitation of a porous oxide scale.
IV. Failure: The corrosive media has oxidized the entire protective coating and has gained access to the alloy underneath, leading to a spallation of the coating.

In relation to these well-known sequences, the HTHC behavior of the ceramic $Ti_{1-x}Al_xN$ coatings is discussed as follows.

3.4.1. Incubation stage

The mechanism starts with the incubation stage, which generally comprises the formation of a passive oxide scale. Particularly for a nitride-based coating, such as $Ti_{1-x}Al_xN$, the growth of a passivating oxide scale is crucial for ensuring their longevity in high-temperature environments. This entails a nitride-to-oxide transformation, which, as discussed in Section 3.2, produces a mixed Al_2O_3/TiO_2 scale under atmospheric conditions (salt-free). Fig. 6a and b show the diffusion profiles of Ti, Al, and O in $Ti_{0.52}Al_{0.48}N$ and $Ti_{0.34}Al_{0.66}N$ coatings after isothermal annealing in an SO_2-rich atmosphere at 850 °C for a duration of 1, 5, 15, and 30 h. While after 1 h, a mixed oxide appears to develop at the coating surface, a gradual separation of Al and Ti is exhibited for longer annealing times. After 30 h, both $Ti_{1-x}Al_xN$ scales follow a layered arrangement, generating an Al-rich layer near the surface and a Ti-rich layer below. This scaling behavior stands in good agreement with works from Panjan et al. [63] and Greczynski et al. [64], who have reported similar results throughout various annealing experiments conducted in air (no additional SO_2).

However, when investigating the HTHC behavior of $Ti_{1-x}Al_xN$ coatings while exposed to a salt deposit, the incubation stage (nitride-to-oxide transformation) occurs simultaneously with the subsequent initiation stage.

3.4.2. Initiation stage

The initiation stage entails a series of changes in the material's environment, which facilitate conditions where further oxidation and/or degradation of the oxide scale occurs. This marks the most crucial step in the HTHC mechanism, as it determines the longevity of the protective coating. For HTHC, such changes include the administration of a salt-deposit, its subsequent solid-to-liquid transformation, the equilibration of the salt-basicity according to the existing temperature and present atmospheric partial pressures, and finally, the formation of a protective oxide by the afore mentioned nitride-to-oxide transformation.

As the salt deposit liquefies, its composition and its character is described by the oxygen partial pressure and the activity of Na_2O (αNa_2O), or the partial pressure of ρSO_3 as it is directly associated with Na_2O by the equilibrium constant in Eq. 11.

$$Na_2SO_4 = pSO_3 + aNa_2O \tag{11}$$

As the thermodynamic equilibrium between SO_2 and SO_3 shifts towards SO_2 with increasing temperature, the equilibrium between Na_2O and SO_3 shifts towards Na_2O, increasing the Na_2O activity and providing a more basic character to the salt deposit. Together with a low ρSO_2 and high ρO_2 in the atmosphere, it is safe to say that the $Ti_{0.52}Al_{0.48}N$-coated samples are exposed to a Na_2SO_4 deposit with a highly basic character.

Regarding the formation of the protective top-oxide, a similar scaling behavior is observed as for salt-free samples, featuring an Al-rich top layer and a Ti-rich sublayer (Figs. 6c and 6d). By revisiting the sequence of the corrosion experiments presented in the experimental section, it was stated that O_2 and SO_2 were added to the atmosphere after the desired temperature of 850 °C and liquefaction of the salt deposit was achieved. Since the solubility of molecular O_2 and SO_2 exhibit poor solubility and slow transport in Na_2SO_4 slags, the observed oxidation of the coating must originate from an ionic O^{2-} transport of the salt-deposit rather than from dissociation and absorption processes out of the gas-phase. This also explains why the oxidation rates (inward diffusion depth) for the salt-loaded samples are much faster (deeper) than for the atmospheric annealing experiments. Conducted under identical thermal and atmospheric conditions, the salt-induced oxidation of the $Ti_{1-x}Al_xN$ coatings solely relies on the ionic diffusion of O^{2-} species from the salt-coating interface (high aNa_2O in basic melts) into the coating and does not rely on the kinetics of oxygen-adsorption, -dissociation and –absorption.

3.4.3. Propagation stage

Now that a top oxide has been established, the HTHC mechanisms transitions into its propagation stage. At this point, an oxygen gradient is established across the liquid film, as the coating has already consumed O^{2-} ions from the salt film, while molecular oxygen from the atmosphere slowly dissolves according to Eq. 12 and diffuses into the melt [36].

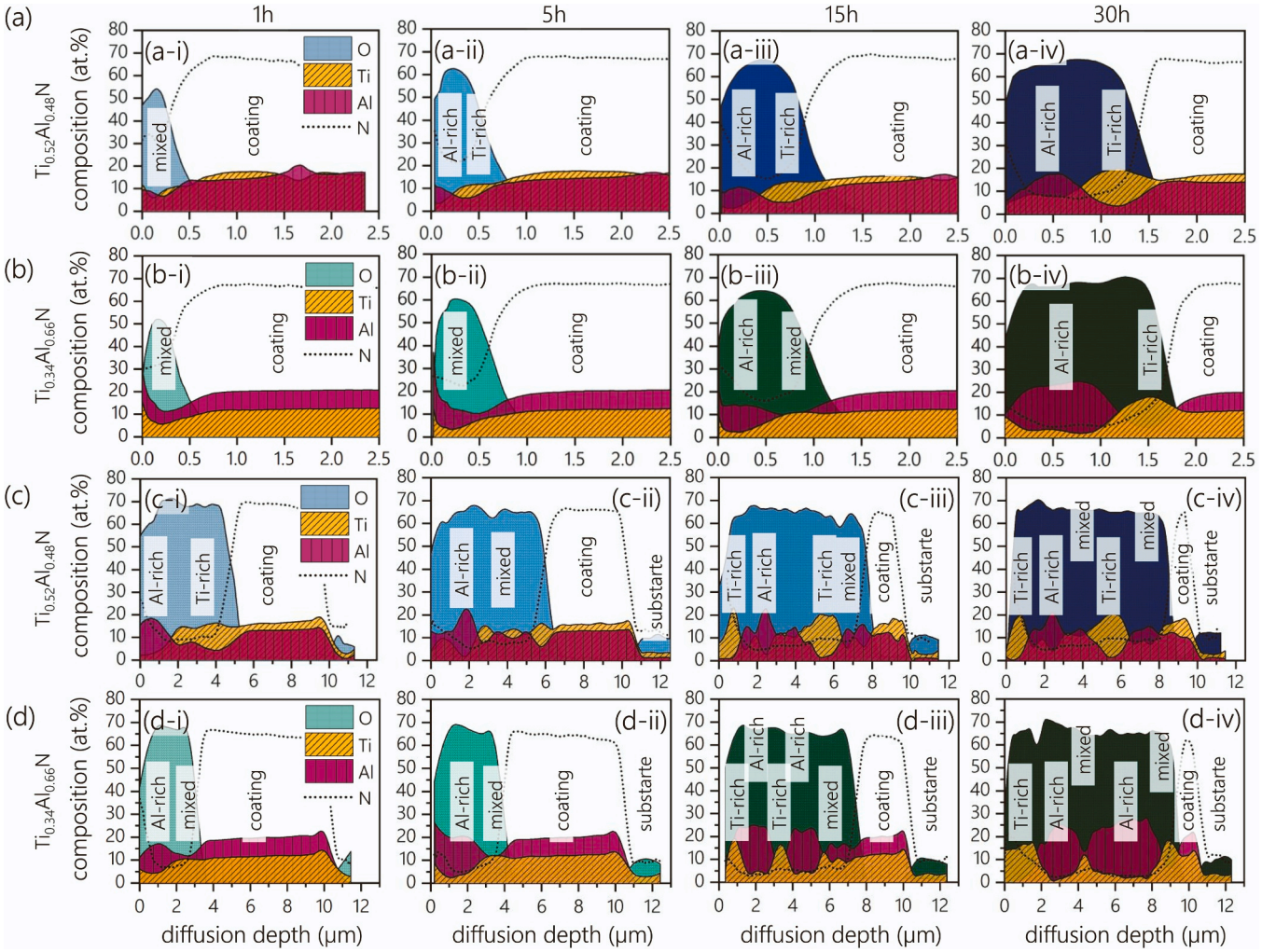

Fig. 6. EDX diffusion profiles highlighting the oxide scale development of salt-free annealed $Ti_{0.52}Al_{0.48}N$ ($a_{i\text{-}iv}$) and $Ti_{0.34}Al_{0.66}N$ coatings ($b_{i\text{-}iv}$), as well as salt-loaded $Ti_{0.52}Al_{0.48}N$ ($c_{i\text{-}iv}$) and $Ti_{0.34}Al_{0.66}N$ ($d_{i\text{-}iv}$) over the course of 30 h.

$$O_2 + 2O^{2-} = 2O_2^{2-} \text{ (dissolution of oxygen in melt)} \quad (12)$$

Therefore, a lower oxygen activity develops at the oxide-melt interface and increases towards the salt-gas interface. For very thin salt films, which can only accommodate a limited amount of O^{2-} as the fluxing mechanisms progress, the activity of sulphur begins to rise at regions of low O^{2-} concentrations, resulting in the sulfidation of unprotected material. In the case of the Ni-based superalloys and other high-temperature alloys with high contents of Cr and Ni, a common feature of HTHC is a precursive sulfide band, which forms at the corrosion front. Kinetically favored in their evolution, non-protective Cr- and Ni-sulfides develop first, after which a corrosive medium can penetrate the porous corrosion scale. Once the O^{2-} activity recovers, the sulfides are oxidized to a porous oxide scale, after which the sulfur activity rises again and reacts with the new unprotected metal below.

This typical progression, however, was not observed throughout this study. As the coating's metal constituents (Ti and Al) are covalently bound to nitrogen, the formation of a metal sulfide band is impeded. Therefore, the propagation stage follows a strict basic fluxing mechanism of repetitive oxidation of the c-Ti(Al)N matrix, followed by the dissolution of its developing oxides. The result is a porous, layered corrosion scale consisting of individual Al-rich and Ti-rich bands. Unlike the dual scale structure obtained when the $Ti_{1-x}Al_xN$ coatings were annealed without a salt deposit, a multitude of porous alternating Ti-rich and Al-rich bands develop. This is clearly illustrated in Figs. 6c and 6d, where EDX depth profiles of the corroded $Ti_{0.52}Al_{0.48}N$ and $Ti_{0.34}Al_{0.66}N$ coatings, respectively, highlight the elemental distribution of Ti, Al, and O after 1, 5, 15 and 30 h. Moreover, a gradual switching of the topmost layer is observed for both coatings. While both coating variants begin to oxidize by developing an Al-rich top-oxide with a Ti-rich oxide layer below, the contribution of the Al-rich layer successively diminishes, and a Ti-rich oxide begins to occupy the topmost layer. This can be attributed to the fact that Al_2O_3 is a highly acidic oxide (Al_2O_3 is more stable under acidic conditions), which is thus more prone to basic fluxing than the more basic TiO_2 oxide (TiO_2 is more stable under basic conditions).

This development of a TiO_2-dominated top-oxide after longer durations of salt exposure (>15 h) is further substantiated by TEM analysis presented in Figs. 7–8. For both $Ti_{1-x}Al_xN$ variants, a highly porous corrosion scale is featured, consisting of five structurally distinct zones that have been highlighted accordingly (zone 1–5) within the STEM cross sections of the $Ti_{0.52}Al_{0.48}N$ (Fig. 7a) and $Ti_{0.34}Al_{0.66}N$ (Fig. 8a) samples. For both coating variants, zone 1 features large grains that have formed at the scale-melt interface and are visible throughout the bright-field images (Fig. 7b-c and Fig. 8b-c). Indexing of the spot patterns that were obtained from the SAED position (b1) render a tetragonal TiO_2-rutile crystal structure (P42/mnm, space group 136), which is consistent for both $Ti_{0.52}Al_{0.48}N$ and $Ti_{0.34}Al_{0.66}N$ top-oxides, as shown in Fig. 7b1* and Fig. 8b1*, respectively.

Positioned directly beneath zone 1 are zones 2–3, which are

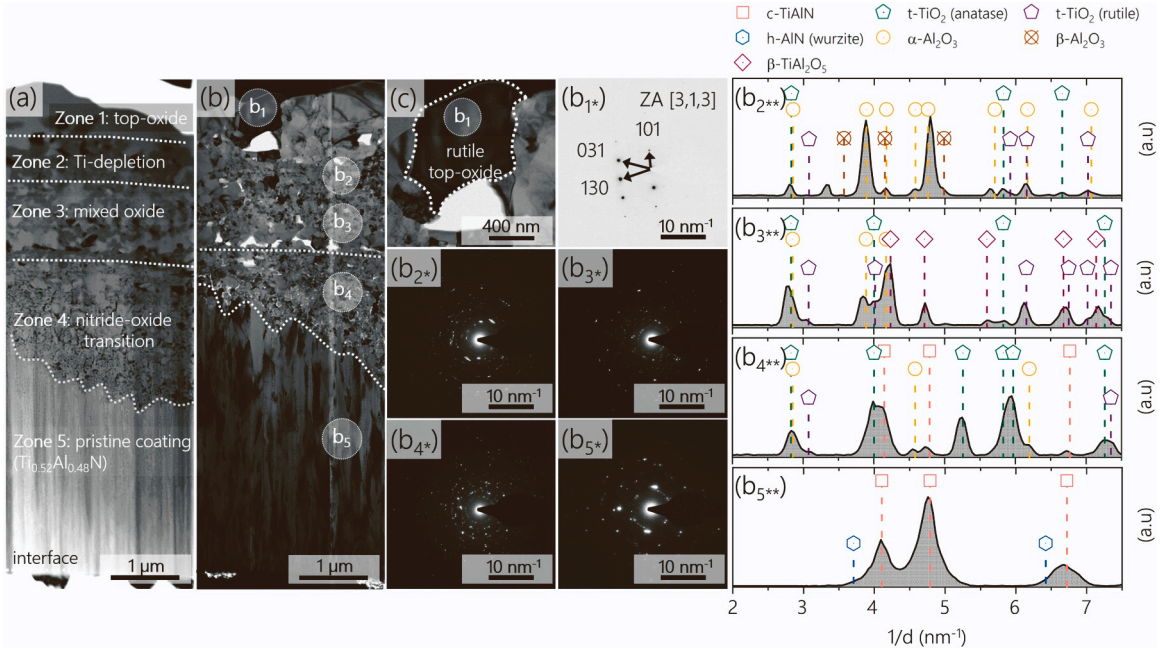

Fig. 7. +TEM investigation featuring progressed hot corrosion of salt-loaded $Ti_{0.52}Al_{0.48}N$ after 15 h at 850 °C. (a) Features a STEM cross-section of the entire $Ti_{0.52}Al_{0.48}N$ coating structure, while (b) shows its TEM bright-field image. Also highlighted in (b) are the locations of five SAEDs (b1-b5), which were taken in order to obtain spacial information of formed oxide phases. Their respective diffractograms are shown seperatelty in (b1*-b5*), while their intensity integration, using CrystBox [65,66], are exhibited in (b2**-b5**). Lastly, (c) shows a close-up bright-field image of the rutile top-oxide scale, which has been indexed as a spot-pattern.

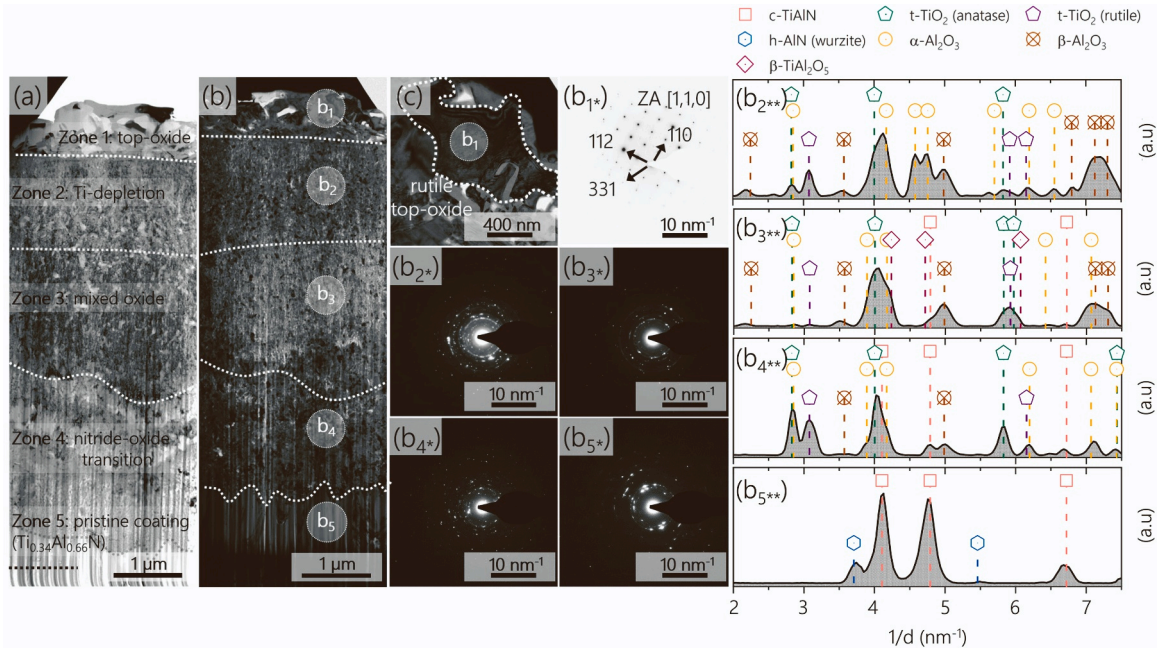

Fig. 8. TEM investigation featuring progressed hot corrosion of salt-loaded $Ti_{0.34}Al_{0.66}N$ after 15 h at 850 °C. (a) Features a STEM cross-section of the entire $Ti_{0.34}Al_{0.66}N$ coating structure, while (b) shows its TEM bright-field image. Also highlighted in (b) are the locations of five SAEDs (b1-b5), which were taken in order to obtain spacial information of formed oxide phases. Their respective diffractograms are shown seperatelty in (b1*-b5*), while their intensity integration, using CrystBox [65,66], are exhibited in (b2**-b5**). Lastly, (c) shows a close-up bright-field image of the rutile top-oxide scale, which has been indexed as a spot-pattern.

characterized by a more refined and marmorated morphology, indicative of a multi-phased crystal structure. Varriations in the granularity of these zones are attributed to the inherently different grain sizes making up both coatings' initial morphologies. That is, an increased granularity of the corrosion scale is produced by the more coarse-grained $Ti_{0.52}Al_{0.48}N$ morphology, while a decreased granularity is obtained due to the more fine-grained $Ti_{0.34}Al_{0.66}N$ structure. By collecting SEADs from zones 2 and 3, intensity profiles were generated by integrating the diffraction intensities and plotting them over the reciprocal of the lattice-spacing. Matching the peak positions to known lattice-spacings of common oxide phases allowed for a more precise description of the corrosion scale and enabled a better understanding of the oxidation behavior of $Ti_{1-x}Al_xN$ coatings under HTHC conditions.

Fig. 7b2** and 8b2** show the intensity plots that pertain to zone 2

of the $Ti_{0.52}Al_{0.48}N$ and $Ti_{0.34}Al_{0.66}N$, respectively. For both $Ti_{1-x}Al_xN$ variants, zone 2 represents a purely oxidized region, where α-Al_2O_3 and β-Al_2O_3 predominantly crystalize, while only minor diffraction intensities relate to Ti-baring oxide phases, such as TiO_2 (rutile & anatase). The lack of Ti species within zone 2 (Ti-depletion layer) can be attributed to an overall outward-directed Ti-diffusion gradient, which produces and stabilizes the outermost TiO_2-rutile top-oxide scale in zone 1. Moreover, significant differences exist between the diffraction patterns within zone 2 obtained from $Ti_{0.52}Al_{0.48}N$ and $Ti_{0.34}Al_{0.66}N$. Probably the most striking difference is the more prominent diffraction contribution by β-Al_2O_3 domains within the high Al-containing $Ti_{0.34}Al_{0.66}N$ coating over its lower Al-containing $Ti_{0.52}Al_{0.48}N$ variant. Being a metastable structure that forms in the presence of sodium aluminate ($NaAl_{11}O_{17}$), the higher Al-content on the metal sublattice within the $Ti_{0.34}Al_{0.66}N$ coating structure seems to benefit the stabilization of the β-Al_2O_3 phase.

Located below zone 2 is zone 3, which has been labeled 'mixed-oxide'. As the name suggests, this zone is characterized by an even distribution of oxide phases, composed of rutile-TiO_2, anatase-TiO_2, α-Al_2O_3, β-Al_2O_3, and also o-$TiAl_2O_5$. It is also the only zone, where the thermally unstable but fast-growing tialite structure (o-$TiAl_2O_5$) develops before it will decompose again into its parent oxides, alumina and rutile. Moreover, zone 3 also exhibits subtle indications of remnant c-Ti(Al)N crystals that have remained unoxidized throughout the corrosion process. This emphasizes that the observed corrosion and scaling behavior is not an entirely homogeneous process, but may vary slightly from position to position.

Zone 4, labeled as 'nitride-oxide-transition', represents the zone closest to the corrosion front, and is characterized by both, significant diffraction intensities by oxide phases, such as TiO_2 and Al_2O_3, but also considerable reflexes related to the c-Ti(Al)N crystal structure. It is here, where the deposited c-Ti(Al)N phase is broken down and oxidized to its respective TiO_2 and Al_2O_3 constituents. Interestingly, this occurs without the seeding of w-AlN domains, nor with fast-growing o-$TiAl_2O_5$ phases. Similar to zones 2–3, the higher Al-containing $Ti_{0.34}Al_{0.66}N$ also produces the metastable β-Al_2O_3 in zone 4, which may explain its presence of in the earlier zones.

Lastly, zone 5 represents the 'pristine coating' morphology and features a state that has remained unimpaired by the corrosive medium. The peak positions from the integrated SAEDs of both coating variants, nicely match the lattice spacings of the c-TiAlN crystal structure and do not reveal any reflexes pertaining to any oxide phase. However, thermally induced spinodal decomposition of the c-$Ti_{1-x}Al_xN$ solid solution renders the precipitation of coherent AlN particles, which has also been observed during XRD analysis. Again, as the $Ti_{0.34}Al_{0.66}N$ chemistry falls closer to the solubility limit of c-Ti(Al)N, more pronounced w-AlN formation is expressed throughout the annealing experiments.

3.5. Time-resolved HTHC scale formation model for $Ti_{1-x}Al_xN$

Finally, a condensed HTHC mechanism is proposed for cae-$Ti_{1-x}Al_xN$ coatings, that has been derived from the previously discussed XRD, EDX, and TEM analyses. Fig. 9 displays several key steps that comprise the most important processes of the HTHC mechanism. At first, the coating is in its as-deposited c-Ti(Al)N state, while exposed to HTHC conditions (850 °C, SO_x-rich atmosphere, and molten Na_2SO_4-$MgSO_4$ salt-deposit), as shown in Fig. 9a. After a relatively short period (< 1 h), the development of a layered oxide scale ensues (Fig. 9b). Its structure consists of an α-Al_2O_3 top-oxide and a subsequent TiO_2-anatase and TiO_2-rutile layer, followed by a $TiAl_2O_5$-tialite-rich mixed oxide layer. Located underneath the tialite-rich layer is the region where the initial nitride is oxidized (nitride-to-oxide transformation) followed by the chemically pristine, but structurally decomposed c-Ti(Al)N coating structure, which now exhibits a dual-phase composition of h-Al(Ti)N and c-Ti(Al)N. Due to the harsh conditions at the coating-salt interface, the growth of a dense and passivating oxide scale is disturbed, yielding a porous structure that allows for accelerated oxide inward diffusion and by extension higher oxidation rates. After longer corrosion times, the previously formed α-Al_2O_3 top-oxide is fluxed according to a basic-fluxing mechanism at the oxide-salt interface (Fig. 9c). Its accelerated deterioration most likely occurs due to its inferior stability in neutral (and alkaline) salt-slags over the competitively growing TiO_2-phases. Furthermore, a sequential layering of Al_2O_3-TiO_2-rich domains develops. It is proposed that this lamellar scaling is promoted by the increased oxygen inward diffusion, the formation of the metastable tialite phase, and finally its subsequent decomposition into its parent oxides Al_2O_3 and TiO_2. Lastly, after longer periods (> 15 h), a fully matured corrosion scale has developed (Fig. 9d). It now consists of a porous TiO_2-rutile top-oxide (being more stable under neutral/alkaline sulfate-salt conditions), and is followed by a lamellar Al_2O_3-TiO_2 oxide scale. At the corrosion front, a mixed-oxide substructure develops due to the nitride-to-oxide transformation of the $Ti_{1-x}Al_xN$ coating structure. Lastly, spinodal decomposition of the metastable c-$Ti_{1-x}Al_xN$ solid solution continues due to the thermal exposure during the corrosion experiments.

4. Conclusion

The present work discusses the HTHC behavior of $Ti_{1-x}Al_xN$ coated c-263 alloy when exposed to a Na_2SO_4/$MgSO_4$ salt mixture, while isothermally annealed at 850 °C in a SO_X-rich atmosphere.

A significant increase in the oxidation kinetics was observed for both, bare c-263 alloy and $Ti_{1-x}Al_xN$ coated samples, when loaded with salt-

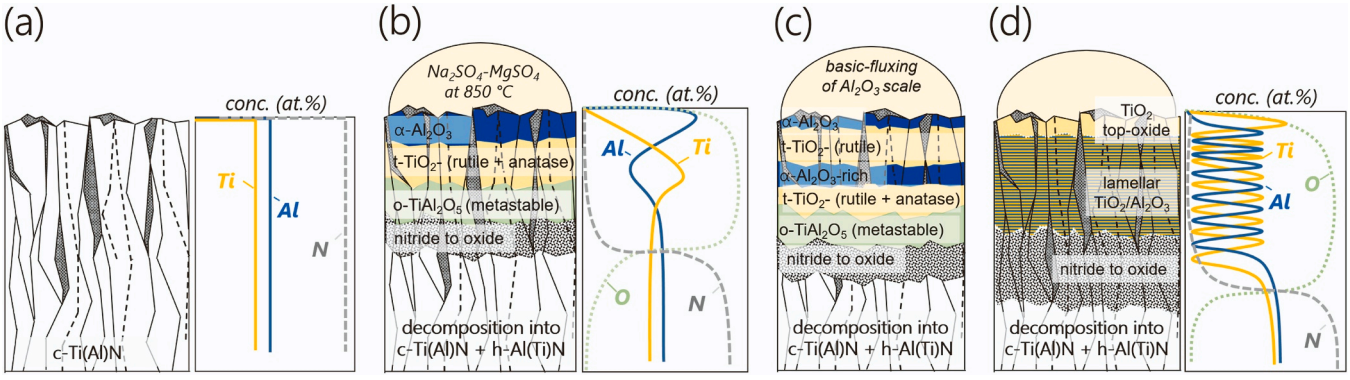

Fig. 9. Proposal of a time-resolved model describing the corrosion scale development of TiAlN-coatings under HTHC conditions. The model features (a) the initial as-deposited c-Ti(Al)N coating with an adherent molten salt-droplet, (b) the nitride-to-oxide transformation resulting in a layered oxide-scale that consits of a Al_2O_3 top-oxide and a TiO_2-rich and metastable $TiAl_2O_5$ sublayer, (c) the basic fluxing of the Al_2O_3 top-oxide and decomposition of the metastable $TiAl_2O_5$ into its parent oxides TiO_2 and Al_2O_3, and (d) the matured corrosion product scale consisting of a rutile top-oxide, a lamellar TiO_2-Al_2O_3 substructure, followed by a porous mixed oxide domain.

deposits during the annealing experiments. While a quasi-cubic rate law (n∼3.0) best describes the oxidation resistance of the bare c-263 alloy and $Ti_{1-x}Al_xN$ coated specimens in absence of a salt-deposit, exposing the speciments to salt accelerated the oxidation kinetics significantly, reaching a compounded parabolic-linear rate law (n=1.5) for the c-263 alloy, and to a parabolic-like rate behavior for the $Ti_{0.52}Al_{0.48}N$ and $Ti_{0.34}Al_{0.66}N$ coated variants (n=2.3 and n=2.2, respectively). According to these findings, a substantially improved corrosion resistance was expressed by the cae-$Ti_{1-x}Al_xN$ samples over the bare c-263 alloy, when salt deposits were introduced to the annealeing experiments in a SO_x-rich atmosphere.

The HTHC mechanism of the $Ti_{1-x}Al_xN$ coatings exhibited a sequential fluxing of Al-rich and Ti-rich domains and found to be the dominating corrosion mechanism, resulting in the formation of a layered and porous corrosion scale. Due to the inherent basic-character of the salt-slag a porous rutile TiO_2 scale predominantly develops at the scale-salt interface, followed by a voluminous Al-rich oxide band below. Depending on the available Al-reservoir of the $Ti_{1-x}Al_xN$, the more pronounced the Al-rich band becomes.

Despite the positive results, showcasing a significant reduction in the corrosion kinetics of TiAlN coated samples over the bare c-263 alloy, the concept of providing HTHC protection through means of cathodic arc evaporation remains the subject of further research.

CRediT authorship contribution statement

Oliver Ernst Hudak: Writing – original draft, Methodology, Investigation, Formal analysis, Data curation, Conceptualization. **Rainer Hahn**: Writing – review & editing, Data curation. **Jürgen Ramm**: Writing – review & editing, Resources. **Tomasz Dipl.-Ing Wojcik**: Investigation, Data curation. **Alexander Scheiber**: Methodology, Conceptualization. **Philip Kutrowatz**: Investigation. **Oliver Hunold**: Resources. **Szilard Kolozsvari**: Writing – review & editing, Resources. **Peter Polcik**: Resources. **Helmut Riedl**: Writing – review & editing, Supervision, Project administration, Funding acquisition.

Declaration of interest statement

The authors declare that they have no known competing financial interests or personal relationships that could have appeared to influence the work reported in this paper.

Data availability

Data will be made available on request.

Acknowledgments

The financial support by the Austrian Federal Ministry for Digital and Economic Affairs, the National Foundation for Research, Technology and Development and the Christian Doppler Research Association is gratefully acknowledged (Christian Doppler Laboratory "Surface Engineering of high-performance Components"). We also thank for the financial support of Plansee SE, Plansee Composite Materials GmbH, and Oerlikon Balzers, Oerlikon Surface Solutions AG. In addition, we want to thank the X-ray center (XRC) of TU Wien for beam time as well as the electron microscopy center - USTEM TU Wien - for providing the TEM facilities. We would like to extend our gratitude to Dr. Eckhardt and VDM Metals International GmbH for their generosity and support throughout this study. Lastly, the authors acknowledge TU Wien library for financial support through its Open Access Funding Program.

References

[1] A.H. Epstein, Aeropropulsion for commercial aviation in the twenty-first century and research directions needed, AIAA J. 52 (2014) 901–911, https://doi.org/10.2514/1.J052713.
[2] A. Poullikkas, An overview of current and future sustainable gas turbine technologies, Renew. Sustain. Energy Rev. 9 (2005) 409–443, https://doi.org/10.1016/j.rser.2004.05.009.
[3] M. Young, H.H. Hanink, New materials for aircraft engines, SAE Tech. Pap. (1943), https://doi.org/10.4271/430133.
[4] A. Czyrska-Filemonowicz, B. Dubiel, M. Ziętara, A. Cetel, Development of single crystal Ni-based superalloys for advanced aircraft turbine blades, Inżynieria Mater. 3–4 (2007) 1–6.
[5] P. Caron, T. Khan, Evolution of Ni-based superalloys for single crystal gas turbine blade applications, Aerosp. Sci. Technol. 3 (1999) 513–523, https://doi.org/10.1016/S1270-9638(99)00108-X.
[6] R. Darolia, Development of strong, oxidation and corrosion resistant nickel-based superalloys: critical review of challenges, progress and prospects, Int. Mater. Rev. 64 (2019) 355–380, https://doi.org/10.1080/09506608.2018.1516713.
[7] F. Pettit, Hot corrosion of metals and alloys, Oxid. Met. 76 (2011) 1–21, https://doi.org/10.1007/s11085-011-9254-6.
[8] G.A. El-Awadi, S. Abdel-Samad, E.S. Elshazly, Hot corrosion behavior of Ni based Inconel 617 and Inconel 738 superalloys, Appl. Surf. Sci. 378 (2016) 224–230, https://doi.org/10.1016/j.apsusc.2016.03.181.
[9] D. Mudgal, S. Singh, S. Prakash, Hot corrosion behavior of some superalloys in a simulated incinerator environment at 900 °C, J. Mater. Eng. Perform. 23 (2014) 238–249, https://doi.org/10.1007/s11665-013-0721-x.
[10] S. Kamal, K.V. Sharma, A.M. Abdul-Rani, Hot corrosion behavior of superalloy in different corrosive environments, J. Miner. Mater. Charact. Eng. 03 (2015) 26–36, https://doi.org/10.4236/jmmce.2015.31004.
[11] J.K. Sahu, B. Ravi Kumar, S.K. Das, N. Paulose, S.L. Mannan, Isothermal high temperature low cycle fatigue behavior of Nimonic-263: influence of type I and type II hot corrosion, Mater. Sci. Eng. A. 622 (2015) 131–138, https://doi.org/10.1016/j.msea.2014.11.016.
[12] B.S. Lutz, J.M. Alvarado-Orozco, L. Garcia-Fresnillo, G.H. Meier, Na2SO4-deposit-induced corrosion of Mo-containing alloys, Oxid. Met. 88 (2017) 599–620, https://doi.org/10.1007/s11085-017-9746-0.
[13] X. Ren, F. Wang, High-temperature oxidation and hot-corrosion behavior of a sputtered NiCrAlY coating with and without aluminizing, Surf. Coat. Technol. 201 (2006) 30–37, https://doi.org/10.1016/j.surfcoat.2005.10.042.
[14] G. Sreedhar, M.M. Alam, V.S. Raja, Hot corrosion behaviour of plasma sprayed YSZ/Al2O3 dispersed NiCrAlY coatings on Inconel-718 superalloy, Surf. Coat. Technol. 204 (2009) 291–299, https://doi.org/10.1016/j.surfcoat.2009.07.026.
[15] R. Jafari, E. Sadeghi, High-temperature corrosion performance of HVAF-sprayed NiCr, NiAl, and NiCrAlY coatings with alkali sulfate/chloride exposed to ambient air, Corros. Sci. 160 (2019) 108066, https://doi.org/10.1016/j.corsci.2019.06.021.
[16] H. Lin, W. Liang, Y. Jia, Q. Miao, R. Hu, Z. Ding, L. Yu, Effect of Al–Y gradient coating on hot corrosion resistance of γ-TiAl alloy at different temperatures, Appl. Surf. Sci. 487 (2019) 868–875, https://doi.org/10.1016/j.apsusc.2019.05.168.
[17] L.K. Wu, J.J. Wu, W.Y. Wu, H.J. Yan, M.Y. Jiang, F.H. Cao, Hot corrosion behavior of electrodeposited SiO2 coating on TiAl alloy, Corros. Sci. 174 (2020) 108827, https://doi.org/10.1016/j.corsci.2020.108827.
[18] R. Li, C. Cheng, J. Pu, NaCl-induced hot-corrosion behavior of TiAlN single-layer and TiAlN/Ti multilayer coatings at 500 °C, Mater. Today Commun. 33 (2022) 104421, https://doi.org/10.1016/j.mtcomm.2022.104421.
[19] M. Zhang, Y. Feng, Y. Wang, Y. Niu, L. Xin, Y. Li, J. Su, S. Zhu, F. Wang, Corrosion behaviors of nitride coatings on titanium alloy in NaCl-induced hot corrosion, Acta Metall. Sin. (Engl. Lett. 34 (2021) 1434–1446, https://doi.org/10.1007/s40195-021-01264-8.
[20] G. Biava, I.B. de Araujo Fernandes Siqueira, R.F. Vaz, G.B. de Souza, H.C. M. Jambo, A. Szogyenyi, A.G.M. Pukasiewicz, Evaluation of high temperature corrosion resistance of CrN, AlCrN, and TiAlN arc evaporation PVD coatings deposited on Waspaloy, Surf. Coat. Technol. 438 (2022) 128398, https://doi.org/10.1016/j.surfcoat.2022.128398.
[21] R.S. Bangari, S. Sahu, P.C. Yadav, Comparative evaluation of hot corrosion resistance of nanostructured AlCrN and TiAlN coatings on cobalt-based superalloys, J. Mater. Res. 33 (2018) 1023–1031, https://doi.org/10.1557/jmr.2018.53.
[22] Y. Qiao, X. Guo, X. Li, Hot corrosion behavior of silicide coating on an Nb-Ti-Si based ultrahigh temperature alloy, Corros. Sci. 91 (2015) 75–85, https://doi.org/10.1016/j.corsci.2014.10.053.
[23] J. He, X. Guo, Y. Qiao, F. Luo, A novel Zr-Y modified silicide coating on Nb-Si based alloys as protection against oxidation and hot corrosion, Corros. Sci. 177 (2020) 108948, https://doi.org/10.1016/j.corsci.2020.108948.
[24] H. Yu, Q. Fan, J. Li, D. Ma, J. Gong, C. Sun, Effect of Si addition to improve the performance of type II and type I hot corrosion resistance of aluminide coating, Corros. Sci. 212 (2023) 110937, https://doi.org/10.1016/j.corsci.2022.110937.
[25] Z. Tang, F. Wang, W. Wu, Effect of Al2O3 and enamel coatings on 900°C oxidation and hot corrosion behaviors of gamma-TiAl, Mater. Sci. Eng. A. 276 (2000) 70–75, https://doi.org/10.1016/S0921-5093(99)00513-4.
[26] H. Zhang, L. Yang, X. Zhang, Q. Wang, J. Wu, Z. Liu, C. Zeng, S. Zhu, Effect of enamel coating on the hot corrosion of 304 stainless steel beneath KCl–ZnCl2 deposits at 450 °C, J. Mater. Res. Technol. 23 (2023) 245–257, https://doi.org/10.1016/j.jmrt.2022.12.152.

[27] R.C. Brown, M.R. Anderson, C.E. Kolb, Aircraft exhaust sulfur emissions, Geogr. Res. Lett. 23 (1996) 3603–3606.
[28] S. Bose. High Temperature Coatings, first ed., Elsevier, 2007, 10.1016/B978-0-7506-8252-7.X5000-8.
[29] E. Yazhenskikh, T. Jantzen, D. Kobertz, K. Hack, M. Müller, Critical thermodynamic evaluation of the binary sub-systems of the core sulphate system Na2SO4–K2SO4–MgSO4–CaSO4, Calphad 72 (2021) 102234, https://doi.org/10.1016/j.calphad.2020.102234.
[30] Z. Rizhang, G. Manjiou, Z. Yu, A study of the mechanism of internal sulfidation-internal oxidation during hot corrosion of Ni-base alloys, Oxid. Met. 27 (1987) 253–265, https://doi.org/10.1007/BF00659270.
[31] R.A. Rapp, Hot corrosion of materials: a fluxing mechanism, Corros. Sci. 44 (2002) 209–221, https://doi.org/10.1016/S0010-938X(01)00057-9.
[32] S. Mrowec, The problem of sulfur in high-temperature corrosion, Oxid. Met. 44 (1995) 177–209, https://doi.org/10.1007/BF01046727.
[33] S. Gialanella, A. Malandruccolo, Aerosp. Alloy. (2020). ⟨http://www.springer.com/series/11054⟩.
[34] H.H. Strehblow, P. Marcus, Fundamentals of corrosion, Corros. Mech. Theory Pract. Third Ed. (2011) 1–104. https://doi.org/10.1002/j.1551-8833.1941.tb19650.x.
[35] A.S. KhannaHigh Temperature Oxidation Elsevier Inc , Second , 2012, , 10.1016/B978-1-4377-3455-3.00005-5.
[36] W. Gao, Z. Li, Developments in High-temperature Corrosion and Protection of Materials, Woodhead Publishing Limited, 2008.
[37] M. Fukumoto, T. Suzuki, M. Sano, M. Hirade, M. Kara, Solubility of metal oxides under control of basicity by electrolysis in fused Na2SO4, Mater. Trans. 45 (2004) 2994–2998, https://doi.org/10.2320/matertrans.45.2994.
[38] A.S. Khanna, High Temperature Oxidation, Handb. Environ. Degrad. Mater. Second Ed. (2012) 127–194. https://doi.org/10.1016/B978-1-4377-3455-3.00005-5.
[39] J.C. Zhao, V. Ravikumar, A.M. Beltran, Phase precipitation and phase stability in Nimonic 263, Metall. Mater. Trans. A Phys. Metall. Mater. Sci. 32 (2001) 1271–1282, https://doi.org/10.1007/s11661-001-0217-4.
[40] O.E. Hudak, A. Scheiber, P. Kutrowatz, T. Wojcik, L. Shang, O. Hunold, S. Kolozsvári, P. Polcik, H. Riedl, Low-temperature hot corrosion of arc evaporated Ti1−xAlxN on Ni-Cr-Co based superalloys, Corros. Sci. 224 (2023), https://doi.org/10.1016/j.corsci.2023.111565.
[41] L. Rogström, J. Ullbrand, J. Almer, L. Hultman, B. Jansson, M. Odén, Strain evolution during spinodal decomposition of TiAlN thin films, Thin Solid Films 520 (2012) 5542–5549, https://doi.org/10.1016/j.tsf.2012.04.059.
[42] International Center of Diffraction Data, Powder diffraction file 04-001-3422, 2011.
[43] International Center of Diffraction Data, Powder diffraction file 00-027-0631, 1972.
[44] International Center of Diffraction Data, Powder diffraction file 04-012-5048, 2011.
[45] International Center of Diffraction Data, Powder diffraction file 00-029-1240, 1978.
[46] International Center of Diffraction Data, Powder diffraction file 01-086-4330, 2020.
[47] International Center of Diffraction Data, Powder diffraction file 01-071-1169, 2020.
[48] International Center of Diffraction Data, Powder diffractoin file 01-080-6097, 2013.
[49] International Center of Diffraction Data, Powder diffraction file 04–015-8610, n.d.
[50] International Center of Diffraction Data, Powder fiffraction file 00-046-1200, 1996.
[51] International Center of Diffraction Data, Powder diffraction file 04-004-8138, 2020.
[52] International Center of Diffraction Data, Powder diffraction file 04-011-9497, 2011.
[53] International Center of Diffraction Data, Powder diffraction file 04-014-3038, 2011.
[54] N. Sheng, K. Horke, A. Meyer, M.R. Gotterbarm, R. Rettig, R.F. Singer, Surface recrystallization and its effect on oxidation of superalloy C263, Corros. Sci. 128 (2017) 186–197, https://doi.org/10.1016/j.corsci.2017.09.020.
[55] D. Fleig, K. Andersson, F. Normann, F. Johnsson, SO 3 formation under oxyfuel combustion conditions, Ind. Eng. Chem. Res. 50 (2011) 8505–8514, https://doi.org/10.1021/ie2005274.
[56] L.P. Belo, L.K. Elliott, R.J. Stanger, R. Spörl, K.V. Shah, J. Maier, T.F. Wall, High-Temperature conversion of SO2 to SO3: homogeneous experiments and catalytic effect of fly ash from air and oxy-fuel firing, Energy Fuels 28 (2014) 7243–7251, https://doi.org/10.1021/ef5020346.
[57] Y. Sarbassov, L. Duan, V. Manovic, E.J. Anthony, Sulfur trioxide formation/emissions in coal-fired air- and oxy-fuel combustion processes: a review, Greenh. Gases Sci. Technol. 0 (2018) 1–27, https://doi.org/10.1002/ghg.1767.
[58] J.P. Dunn, P.R. Koppula, H. G. Stenger, I.E. Wachs, Oxidation of sulfur dioxide to sulfur trioxide over supported vanadia catalysts, Appl. Catal. B Environ. 19 (1998) 103–117, https://doi.org/10.1016/S0926-3373(98)00060-5.
[59] J. hua HE, X. ping GUO, Y. qiang QIAO, Oxidation and hot corrosion behaviors of Nb−Si based ultrahigh temperature alloys at 900 °C, Trans. Nonferrous Met. Soc. China (Engl. Ed. 31 (2021) 207–221, https://doi.org/10.1016/S1003-6326(20)65488-7.
[60] Z. Lin, M. Li, J. Wang, Y. Zhou, Microstructure and high-temperature corrosion behavior of a Cr-Al-C composite, J. Am. Ceram. Soc. 90 (2007) 3930–3937, https://doi.org/10.1111/j.1551-2916.2007.02059.x.
[61] G.C. Fryburg, F.J. Kohl, C.A. Stearns, W.L. Fielder, Chemical reactions involved in the initiation of hot corrosion of B-1900 and NASA-TRW VIA, J. Electrochem. Soc. 129 (1982) 571–585, https://doi.org/10.1149/1.2123928.
[62] J. Stringer, High-temperature corrosion of superalloys, Mater. Sci. Technol. 3 (1986) 482–493, https://doi.org/10.1080/02670836.1987.11782259.
[63] P. Panjan, B. Navinšek, M. Čekada, A. Zalar, Oxidation behaviour of TiAlN coatings sputtered at low temperature, Vacuum 53 (1999) 127–131, https://doi.org/10.1016/S0042-207X(98)00407-2.
[64] G. Greczynski, L. Hultman, M. Odén, X-ray photoelectron spectroscopy studies of Ti1-xAlxN ($0 \leq x \leq 0.83$) high-temperature oxidation: the crucial role of Al concentration, Surf. Coat. Technol. 374 (2019) 923–934, https://doi.org/10.1016/j.surfcoat.2019.06.081.
[65] M. Klinger, A. Jäger, Crystallographic tool box (CrysTBox): automated tools for transmission electron microscopists and crystallographers, J. Appl. Crystallogr. 48 (2015) 2012–2018, https://doi.org/10.1107/S1600576715017252.
[66] M. Klinger, More features, more tools, more CrysTBox, J. Appl. Crystallogr. 50 (2017) 1226–1234, https://doi.org/10.1107/S1600576717006793.